

See discussions, stats, and author profiles for this publication at: <https://www.researchgate.net/publication/263981673>

Ordered Phases of Reduced Ceria As Epitaxial Films on Cu(111)

ARTICLE in THE JOURNAL OF PHYSICAL CHEMISTRY C · DECEMBER 2013

Impact Factor: 4.77 · DOI: 10.1021/jp409220p

CITATIONS

11

READS

47

11 AUTHORS, INCLUDING:



[Mykhailo Vorokhta](#)

Charles University in Prague

32 PUBLICATIONS 211 CITATIONS

SEE PROFILE



[Daniel Mazur](#)

Charles University in Prague

19 PUBLICATIONS 102 CITATIONS

SEE PROFILE



[Iva Matolínová](#)

Charles University in Prague

65 PUBLICATIONS 725 CITATIONS

SEE PROFILE



[Vladimír Matolín](#)

Charles University in Prague

285 PUBLICATIONS 3,013 CITATIONS

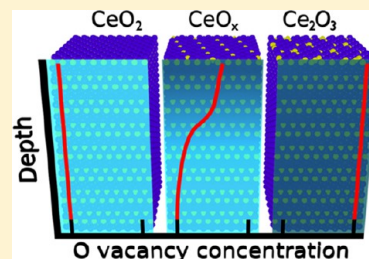
SEE PROFILE

Ordered Phases of Reduced Ceria As Epitaxial Films on Cu(111)

Tomáš Duchoň, Filip Dvořák, Marie Aulická, Vitalii Stetsovych, Mykhailo Vorokhta, Daniel Mazur, Kateřina Veltruská, Tomáš Skála, Josef Mysliveček,* Iva Matolínová, and Vladimír Matolín

Faculty of Mathematics and Physics, Department of Surface and Plasma Science, Charles University in Prague, V Holešovičkách 2, 18000 Praha 8, Czech Republic

ABSTRACT: Changes of stoichiometry in reducible oxides are inevitably accompanied by changes of the oxide structure. We study the relationship between the stoichiometry and the structure in thin epitaxial films of reduced ceria, CeO_x , $1.5 \leq x \leq 2$, prepared via an interface reaction between a thin ceria film on Cu(111) and a Ce metal deposit. We show that the transition between the limiting stoichiometries CeO_2 and Ce_2O_3 is realized by equilibration of mobile oxygen vacancies near the surface of the film, while the fluorite lattice of cerium atoms remains unchanged during the process. We identify two surface reconstructions representing distinct oxygen vacancy ordering during the transition, a $(\sqrt{7} \times \sqrt{7})\text{R}19.1^\circ$ reconstruction representing a bulk termination of the $\iota\text{-Ce}_7\text{O}_{12}$ and a (3×3) reconstruction representing a bulk termination of $\text{CeO}_{1.67}$. Due to the special property to yield ordered phases of reduced ceria the interface reaction between Ce and thin film ceria represents a unique tool for oxygen vacancy engineering. The perspective applications include advanced model catalyst studies with both the concentration and the coordination of oxygen vacancies precisely under control.



INTRODUCTION

Reducible oxides play an important role in heterogeneous catalysis.^{1–7} Due to their ability to store or release oxygen, reducible oxides usually act as an oxygen supply or a reducing agent during catalytic reactions.^{8,9} Reactions over reducible oxides are typically accompanied by changes in the oxide stoichiometry that are often realized on complex phase diagrams^{10–17} and may influence the catalytic activity through changes in local coordination, surface termination, and long-range ordering in the oxide.^{18–21} Model studies isolating the changes of the oxide stoichiometry are of the utmost importance for understanding the role of stoichiometry in the reaction mechanisms over reducible oxides and for improving and developing new catalysts.

The reactivity of cerium oxide-based catalysts is greatly influenced by the presence of oxygen vacancies in ceria.^{22,23} The ability to adjust the concentration and the distribution of oxygen vacancies allows for the control over the reactivity and the selectivity of ceria-based catalysts.^{24,25} For this reason, having experimental access to ordered phases of cerium oxide with different concentration and coordination of oxygen vacancies greatly enhances the possibilities of model catalytic studies. Several phases of ordered reduced ceria have been prepared in the past in the form of powder or single-crystal samples,^{26–28} but only recently ordered reduced phases of ceria have been realized in the form of thin films on single crystalline supports. The thin film of the $\iota\text{-Ce}_7\text{O}_{12}$ phase on hex- $\text{Pr}_2\text{O}_3(0001)/\text{Si}(111)$ substrate was obtained by Wilkens et al. via heating of the CeO_2 layer in vacuum.²⁹ A thin film of the $c\text{-Ce}_2\text{O}_3$ phase on Cu(111) was obtained by our group via an alternative method of reducing the CeO_2 layer in an interface reaction with metallic Ce.³⁰ The thin film of the $c\text{-Ce}_2\text{O}_3$ phase

has been reported also in the latest study on hex- $\text{Pr}_2\text{O}_3(0001)/\text{Si}(111)$.³¹

Here we present a detailed investigation of the properties of the ceria layers on Cu(111) reduced by the interface reaction with Ce. Using a stepwise titration of ceria layers with Ce in the interface reaction, we continuously change the stoichiometry of the ceria layers on Cu(111) from CeO_2 ³² to Ce_2O_3 .³⁰ We characterize the concentration and the depth profile of the oxygen vacancies in the reduced ceria layers by photoelectron spectroscopy (XPS) and resonance photoelectron spectroscopy (RPES), the surface reconstruction of the layers by low-energy electron diffraction (LEED), the morphology of the layers by scanning tunneling microscopy (STM), and the surface composition of the layers by ion scattering spectroscopy (ISS). We are identifying two surface reconstructions of ordered reduced ceria on Cu(111)—the $(\sqrt{7} \times \sqrt{7})\text{R}19.1^\circ$ reconstruction corresponding to bulk $\iota\text{-Ce}_7\text{O}_{12}$ ²⁹ and the (3×3) reconstruction corresponding to bulk $\text{CeO}_{1.67}$. We show that the process of reduction of ceria via the interface reaction with metallic Ce is fully reversible upon oxidation by O_2 . This allows us to interpret the properties of the reduced ceria films in our experiment in terms of creation, annihilation, and equilibration of oxygen vacancies in the fluorite lattice of cubic ceria. Reduction of ceria thin films by metallic Ce complemented by oxidation by O_2 allows a precise experimental control over both the concentration and the coordination of oxygen vacancies in thin ceria films. The coordination of oxygen vacancies represents a new degree of freedom that can be controlled

Received: September 15, 2013

Revised: December 5, 2013

Published: December 9, 2013



and exploited for example in advanced model catalytic studies over ceria.

■ EXPERIMENTAL SECTION

Experiments were carried out in three ultrahigh vacuum systems with a base pressure of 1×10^{-8} Pa. All systems are equipped with the necessary sample cleaning and in situ preparation facilities, low electron energy diffraction (LEED) optics, laboratory X-ray sources, and X-ray photoelectron spectroscopy (XPS) analyzers. One of the apparatuses is located at the Materials Science Beamline in Trieste representing a tunable X-ray source for resonance photoelectron spectroscopy (RPES). Another apparatus is equipped with scanning tunneling microscopy (STM) and the third one with ion scattering spectroscopy (ISS). Prior to the sample preparation, the Cu(111) single-crystal substrate (MaTeck) was cleaned by several cycles of Ar⁺ sputtering and annealing in vacuum, and the Ce evaporator was thoroughly degassed. As a starting point for the experiment, layers of CeO₂(111) on Cu(111) with a typical thickness of 3 nm were prepared by evaporating Ce (Goodfellow, 99.9%) from a tantalum or molybdenum crucible heated by electron bombardment in a background atmosphere of 5×10^{-5} Pa of O₂ (Linde, 5.0) and at substrate temperature of 250 °C.³² Reduction of the prepared CeO₂(111) buffers was achieved through deposition of metallic cerium without oxygen background and subsequent annealing at 600 °C for 30 min in vacuum. Oxidation of the layers was performed by exposure to controlled doses of O₂ at room temperature and subsequent annealing at 600 °C for 30 min in vacuum. The reduction and oxidation steps were eventually repeated or alternated to obtain the desired ordering and stoichiometry of the layers. Typically, the reduction step involves a deposition of 0.5 nm of Ce and the oxidation step a dose of O₂ as small as 1 L.

The thickness of the prepared ceria films was determined from the attenuation of the Cu 2p_{3/2} signal of the substrate measured by XPS. The attenuation length for CeO₂ and Ce₂O₃ was calculated using the TPP-2 M formula.³³ The reference for ceria coverage in this work is 1 monolayer (ML), a stack of O–Ce–O layers corresponding to the vertical stacking of O and Ce in (111) direction in fluorite-like phases of ceria. One ML is 3.1 Å thick and contains 7.9×10^{14} cm⁻² Ce atoms. Identification of the particular ordered reduced phases of ceria in different apparatuses was achieved based on the combination of the characteristic LEED diffraction patterns and XPS spectra of Ce 3d and O 1s. XPS spectra of Ce 3d, Cu 2p_{3/2}, and O 1s core levels were recorded using the excitation energy of $h\nu = 1486.6$ eV (Al K α). The characteristic properties of the reduced ceria layers presented in this article were repeatedly observed in about 30 experiments.

The main information obtained from the photoelectron spectroscopy measurements is the degree of reduction of the ceria layers. Creation of one oxygen vacancy in CeO_x is accompanied by localization of two excess electrons on two lattice Ce ions changing their charge state from Ce⁴⁺ to Ce³⁺.⁹ We determine the concentration of Ce³⁺ and Ce⁴⁺ in XPS from the areas Ce³⁺_{area} and Ce⁴⁺_{area} of Ce³⁺ and Ce⁴⁺ features in the Ce 3d spectra, respectively, identified and fitted according to Skála et al.³⁴ The accuracy of this method in the determination of the Ce³⁺ and Ce⁴⁺ concentrations is $\pm 2\%$, and the method is able to detect changes of the Ce³⁺ and Ce⁴⁺ concentrations between two samples as small as $\pm 0.5\%$.³⁵ We describe the degree of reduction by a ratio $\text{Ce}^{3+}_{\text{area}}/(\text{Ce}^{3+}_{\text{area}} + \text{Ce}^{4+}_{\text{area}})$ or by x in the

notation CeO_x. The degree of reduction obtained from XPS represents a weighted average over the information depth of XPS measurements. For XPS of Ce 3d, Al K α , and the detection of photoelectrons along the sample normal the information depth is about 3 nm or 10 ML. To obtain more surface-sensitive information we additionally perform XPS measurements 70° off the sample normal decreasing the information depth, theoretically, by $\cos 70^\circ$, i.e., a factor of 3.³⁶

For the highest surface sensitivity, we performed RPES measurements of the valence band of the ceria samples using synchrotron radiation.³⁷ For determining the degree of reduction from RPES, we use the resonance enhancement D(Ce⁴⁺) and D(Ce³⁺) of Ce⁴⁺ and Ce³⁺ features in the RPES spectra (ref 37, cf. Figure 4) assuming a direct proportionality of D(Ce⁴⁺) and D(Ce³⁺) to the concentration of Ce⁴⁺ and Ce³⁺ ions.³⁸ The used photon energies were 115 eV for off resonance, 124.8 eV for Ce⁴⁺ resonance, and 121.4 eV for Ce³⁺ resonance measurements.

The surface composition of the samples was determined with ISS.³⁰ He⁺ ions with the energy of 2 keV and the impact angle of 45° were used for the measurements. The LEED, XPS, RPES, and ISS measurements were carried out at room temperature upon a flash heating of the sample to 500 °C to minimize the effects of eventual unintended adsorption, namely, OH groups. Heating of the samples was not available for STM measurements. STM images were obtained at room temperature by tunneling of electrons into empty states of the sample using chemically etched and vacuum-annealed tungsten tips.

■ EXPERIMENTAL RESULTS

Our experiments demonstrate that controlling the amount of Ce deposit in the interfacial reaction of metallic Ce with a ceria film allows preparation of reduced CeO_x films in the range of $1.5 \leq x \leq 2$. The change of the stoichiometry determined from XPS measurements is continuous; however, we are able to identify four characteristic surface reconstructions in our layers. The electron diffractograms of these reconstructions are shown in Figure 1. Starting from the (1 × 1) reconstruction of the CeO₂(111) surface (Figure 1(a), ref 32) the increasing degree of reduction of the ceria layer is accompanied by the change of the LEED pattern to $(\sqrt{7} \times \sqrt{7})R19.1^\circ$ (Figure 1(b)), (3 × 3) (Figure 1(c)), and finally (4 × 4) reconstruction of c-Ce₂O₃(111) (Figure 1(d), ref 30). The samples showing a single set of LEED spots as in Figure 1 are carefully prepared to certain narrow ranges of the CeO_x stoichiometry. We consider the properties of such samples as characteristic of the evolution of the reduction of CeO_x thin films on Cu by Ce and only refer to the samples showing the single set of LEED spots in this work (Figures 1–5). For stoichiometries outside the narrow characteristic ranges the samples show typically a combination of two sets of LEED spots from Figure 1 indicating a coexistence of the reconstructions on the surface.

The stoichiometry of the films prepared by interfacial reaction has been followed by XPS, with the degree of reduction of the samples characterized through fitting of the measured Ce 3d spectra.³⁴ The Ce 3d and O 1s spectra measured on the samples exhibiting LEED patterns as in Figure 1 are shown in the lower part of Figure 2 (“Ce deposition”). The ratios $\text{Ce}^{3+}/(\text{Ce}^{3+} + \text{Ce}^{4+})$ determined from the curves in Figure 2 are plotted in Figure 3. The starting CeO₂ buffer exhibits only features of Ce⁴⁺. The increase of the amount of metallic Ce in the interfacial reaction between Ce and CeO₂

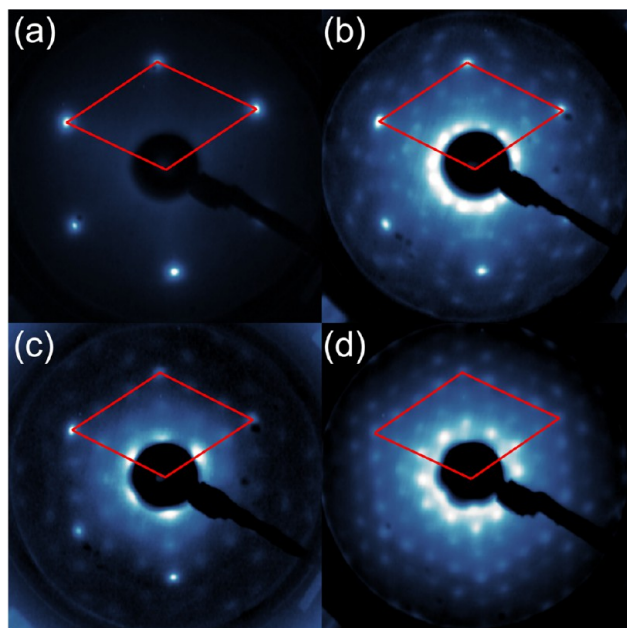


Figure 1. LEED images of ordered phases of reduced ceria on Cu(111) obtained by interface reaction of the $\text{CeO}_2(111)$ buffer layer with Ce deposit. Degree of reduction increases from (a) to (d). (a) (1×1) spots of $\text{CeO}_2(111)$ buffer layer, (b) $(\sqrt{7} \times \sqrt{7})\text{R}19.1^\circ$ reconstruction, (c) (3×3) reconstruction, (d) (4×4) reconstruction of $c\text{-Ce}_2\text{O}_3$. Electron energy 58 eV. The (1×1) unit cell of $\text{CeO}_2(111)$ is outlined red.

leads to the increase in contribution of the Ce^{3+} features to the spectra.³⁴ By increasing the amount of metallic Ce the stoichiometry of the layers after reaction can be tuned from pure CeO_2 to pure Ce_2O_3 . Apart from the changes in Ce 3d spectra this transition is accompanied by a shift of the O 1s line to higher binding energies^{30,39} as shown in Figure 2.

An important insight into the oxidation–reduction properties of ordered layers of reduced ceria can be obtained by oxidation of the samples by O_2 after reaching the limiting stoichiometry of Ce_2O_3 , LEED pattern (4×4) . Oxidation by O_2 allows changing the stoichiometry of the reduced ceria layers from Ce_2O_3 back to CeO_2 with all the characteristic surface reconstructions of ordered reduced ceria identified by LEED (Figure 1) observed during oxidation as well. The Ce 3d and O 1s spectra measured on the samples upon oxidation of the Ce_2O_3 layers are shown in the upper part of Figure 2 (“ O_2 exposure”).

The XPS spectra for all samples were measured at two angles of photoelectron emission: 0° and 70° off sample normal (cf. Figure 2). The difference between the two signals can be used as an indication of enhancement of concentration of the measured features near the surface of the layer. The results for all surface reconstructions are summarized in Figure 3, where the difference between the degree of sample reduction measured for 0° emission and 70° emission is marked gray. While the samples with the limiting stoichiometry CeO_2 (1×1) and Ce_2O_3 (4×4) show small or no difference in the degree of reduction,³⁰ the layers with intermediate stoichiometry $(\sqrt{7} \times \sqrt{7})\text{R}19.1^\circ$ and (3×3) show an enhancement of the Ce^{3+} signal and, consequently, oxygen vacancy concentration near the surface of the layer. This gradient of the vacancy concentration with depth below the surface is observed in all samples with intermediate stoichiometry. The oxygen vacancies

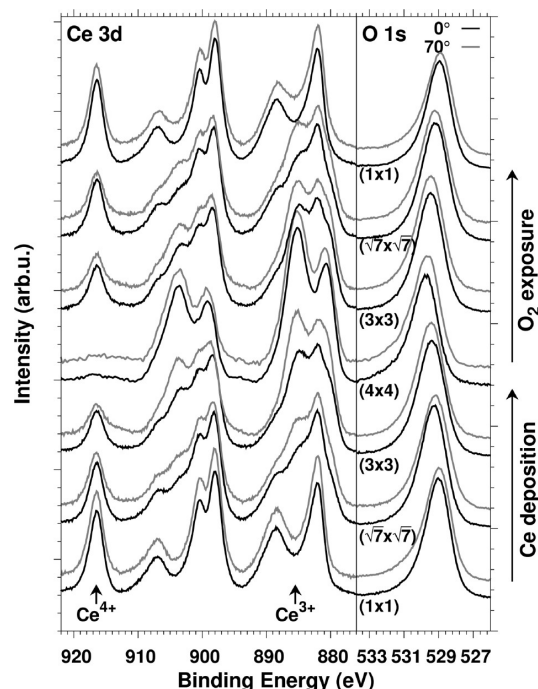


Figure 2. XPS spectra belonging to the ordered phases of reduced ceria on Cu(111). Left panel: Ce 3d. Right panel: O 1s. Samples measured at 0° (black curves) and 70° off-normal emission (gray curves). With each sample the corresponding LEED pattern is indicated. (1×1) is the starting CeO_2 layer. Bottom $(\sqrt{7} \times \sqrt{7})\text{R}19.1^\circ$, (3×3) , and (4×4) samples were obtained by reduction of $\text{CeO}_2(111)$ layers via interface reaction with Ce. Top (3×3) , $(\sqrt{7} \times \sqrt{7})\text{R}19.1^\circ$, and (1×1) samples were obtained by oxidation of the (4×4) $c\text{-Ce}_2\text{O}_3(111)$ layers with O_2 . The areas of the presented spectra have been normalized to 1 after subtraction of Shirley background, and the curves have been offset for clarity. For better orientation, the positions of visually the most prominent peaks in Ce^{4+} and Ce^{3+} spectra are marked by arrows.

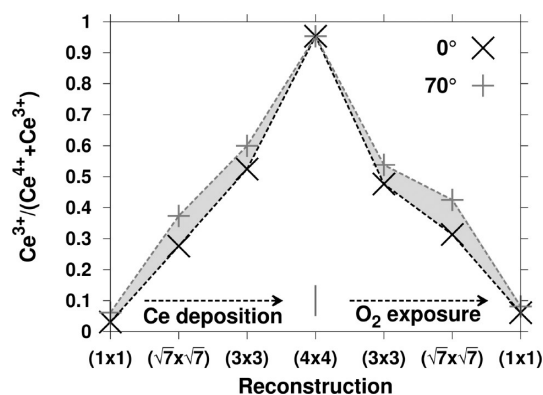


Figure 3. Degree of reduction of the ordered phases of reduced ceria on Cu(111) obtained by fitting of the XPS spectra from Figure 2. Vertical axis: degree of reduction. Horizontal axis: surface structure. Surface structures were obtained by reduction of $\text{CeO}_2(111)$ layers via interface reaction with Ce (left) or by oxidation of $c\text{-Ce}_2\text{O}_3(111)$ layers with O_2 (right). The difference between the degree of reduction measured with normal emission (black crosses) and with 70° off-normal emission (gray crosses) indicating the accumulation of oxygen vacancies near the surface of $(\sqrt{7} \times \sqrt{7})\text{R}19.1^\circ$ and (3×3) surface structures is enhanced by light gray. The dashed lines are guides to the eyes.

accumulate near the surface of the layers regardless of the particular preparation method, both after reduction with Ce and after oxidation with O₂.

While the LEED images define the observed surface reconstructions without ambiguity, the degree of reduction observed in the XPS spectra for ceria layers with intermediate stoichiometry strongly depends on the thickness of the ceria layers. The reason for the dependence of the XPS spectra on the thickness of the layer is the averaging over different but finite thickness of the layer in the presence of the gradient of the vacancy concentration together with eventual modifications of the Ce³⁺ concentration near the interface with the metal substrate.⁴⁰ For comparability of the XPS spectra, the samples presented in Figure 2 have been selected to have a thickness of about 4 nm after preparation. Ceria layers work as a supply or a sink of oxygen during reduction by Ce or oxidation by O₂, respectively, so the amount of Ce and the doses of O₂ needed to reach the desired stoichiometry of the layer depend sensitively on the thickness of the layers, too. Particularly, the samples in Figure 2 were prepared with reaction parameters summarized in Table 1. For the layers prepared by interface

Table 1. Parameters of the Preparation of the Samples From Figures 2 and 3

reconstruction	reduction by Ce		oxidation by O ₂	
	thickness of the CeO ₂ buffer	thickness of the reacted layer	thickness of the Ce ₂ O ₃ layer	O ₂ dose
(1 × 1)	3.0 nm	-	4.2 nm	10000 L
($\sqrt{7} \times \sqrt{7}$)R19.1°	3.5 nm	4.0 nm	4.5 nm	20 L
(3 × 3)	3.0 nm	3.7 nm	4.4 nm	1 L
(4 × 4)	3.0 nm	4.2 nm	-	-

reaction between CeO₂ buffer and Ce, the thickness of the starting CeO₂ buffer and the thickness of the resulting layer after reaction are listed. For the layers prepared by oxidation of Ce₂O₃ layers, the thickness of the starting Ce₂O₃ layer and the exposure of O₂ are listed. Given the small difference between the XPS attenuation lengths for CeO₂ and Ce₂O₃,³³ the amount of Ce in the interfacial reaction calculates straightforwardly from the difference between the initial and the final thickness of the layer. Upon oxidation, the thickness of the layers does not change significantly. For thicknesses of the layers other than ≈4 nm, the amount of Ce and/or doses of O₂ for obtaining a desired reconstruction must be determined in a dedicated experiment.

The resonance photoelectron spectroscopy of the valence band is a more surface-sensitive probe of the stoichiometry than the XPS because kinetic energies of the analyzed photoelectrons are lower than for XPS of Ce 3d (115 and 600 eV, respectively).³⁶ The RPES signal is thus more closely related to the surface reconstructions observed in LEED. RPES spectra of the valence band for the samples with the LEED patterns and the XPS spectra corresponding to Figures 1 and 2, respectively, are shown in Figure 4. The limiting cases of CeO₂ and Ce₂O₃ show only resonance enhancement D(Ce⁴⁺) and D(Ce³⁺), respectively, as is the case published in ref 30. The intermediate samples show a mixture of both contributions, with D(Ce³⁺) being slightly higher on the (3 × 3) reconstructed sample. The degree of reduction $D(\text{Ce}^{3+})/(D(\text{Ce}^{3+}) + D(\text{Ce}^{4+}))$ equals to 0.65 and 0.71 for ($\sqrt{7} \times \sqrt{7}$)R19.1° and (3 × 3) reconstructed samples yielding closely spaced stoichiometries of CeO_{1.65} and

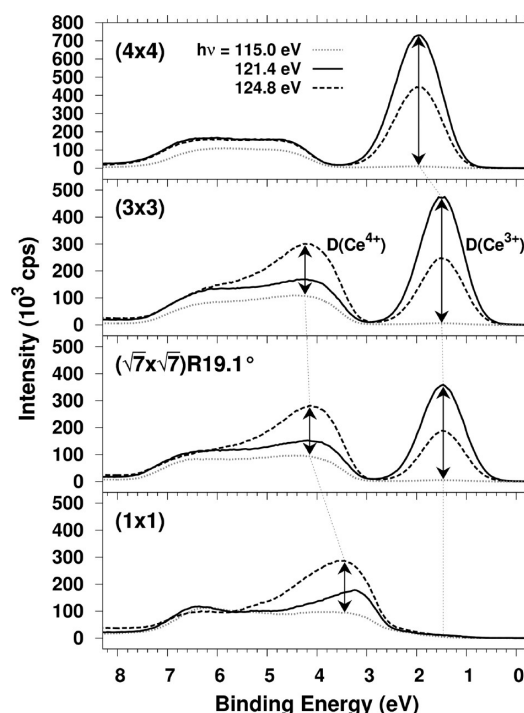


Figure 4. RPES spectra of the valence band of the ordered phases of reduced ceria on Cu(111). With each sample the corresponding LEED pattern is indicated. The spectra are measured off-resonance (photon energy 115 eV, dotted lines), in the Ce⁴⁺ resonance (124.8 eV, dashed lines), and in the Ce³⁺ resonance (121.4 eV, full lines). The resonance enhancements D(Ce³⁺) and D(Ce⁴⁺) are indicated by arrows.

CeO_{1.65} for the near surface regions of ($\sqrt{7} \times \sqrt{7}$)R19.1° and (3 × 3) reconstructed samples. The reduction of the samples is accompanied by a shift to higher binding energies of the Ce 4f and O 2p valence region features observed in RPES which is in accordance with the previously published data on oxidation of Ce.⁴¹

The morphology of the reduced ceria films has been determined by STM. Ceria layers reduced by interface reaction with metallic Ce show a very good ordering due to the interface reaction.³⁰ The CeO₂ buffer layer shows a typical average terrace width of 10 nm (Figure 5(a)) corresponding to the growth temperature of 250 °C.³² After the reaction with Ce and annealing at 600 °C, the resulting c-Ce₂O₃ film exhibits an increased average terrace width of 30 nm (Figure 5(c)). Ordered film with average terrace width of 30 nm is observed also for ceria layers with ($\sqrt{7} \times \sqrt{7}$)R19.1° reconstruction (Figure 5(b)) as well as for the layers with the (3 × 3) reconstruction (not shown). Subsequent oxidation of the ceria films by oxygen does not greatly change the film morphology. On the c-Ce₂O₃ samples exposed to 10 000 L of O₂ (Figure 5(d)), the average terrace width remains without change. Occasionally deep troughs in the oxidized layers are observed. We interpret the troughs as cracks resulting from stress release in the layer during oxidation when the lattice parameter of the ceria is decreasing.³⁰

The cracks in the ceria layers after oxidation may strongly affect the chemical reactivity of the ceria layers in model catalytic studies by exposing the very active ceria–copper interface to the reactants.⁴² To assess the availability of the ceria–copper interface in our samples from Table 1 we determine the amount of the exposed Cu by ISS. The starting CeO₂ buffer prepared at 250 °C with the thickness of

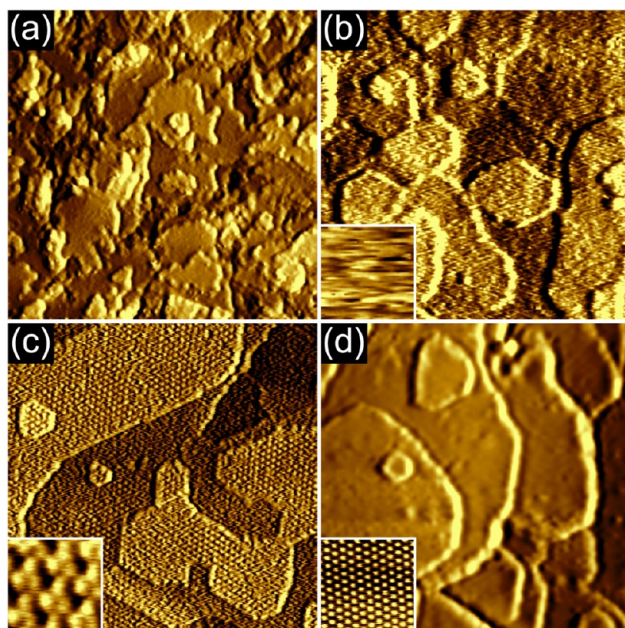


Figure 5. STM micrographs illustrating the morphology of cerium oxide films during reduction and reoxidation. (a) As-prepared fully oxidized buffer layer of CeO_2 . (b) Ceria layer with $(\sqrt{7} \times \sqrt{7})\text{R}19.1^\circ$ surface reconstruction prepared via interface reaction of metallic Ce with CeO_2 buffer layer. Inset: The instability of the tunneling contact inherent to the $(\sqrt{7} \times \sqrt{7})\text{R}19.1^\circ$ surface reconstruction causes the streaky appearance of the layer. The morphology and the instability of the tunneling contact of the layers with (3×3) surface reconstruction is the same as in (b). (c) $c\text{-Ce}_2\text{O}_3$ layer prepared via interface reaction of metallic Ce with the CeO_2 buffer layer. Inset: high-resolution image of the (4×4) surface reconstruction of $c\text{-Ce}_2\text{O}_3$. (d) CeO_2 film obtained by oxidation of the $c\text{-Ce}_2\text{O}_3$ layer. Inset: high-resolution image of the (1×1) reconstruction of CeO_2 . Size of images is $75 \times 75 \text{ nm}^2$, size of insets $4 \times 4 \text{ nm}^2$.

approximately 3 nm yields a Cu signal at the detection limit of the ISS of $\leq 0.2\%$ ML Cu (1 ML Cu represents $1.8 \times 10^{15} \text{ cm}^{-2}$ Cu atoms). On the layers with the thickness of approximately 4 nm and the $(\sqrt{7} \times \sqrt{7})\text{R}19.1^\circ$, (3×3) , and (4×4) reconstructions prepared by deposition of Ce and the interfacial reaction on the CeO_2 buffer, the Cu signal is not measurable by ISS. On the contrary, the layers with (3×3) , $(\sqrt{7} \times \sqrt{7})\text{R}19.1^\circ$, and (1×1) reconstructions prepared by oxidation of the layers with the (4×4) reconstruction yield Cu signals between 0 and 2% ML Cu. Thus, the layers of ordered reduced ceria obtained in our experiment by interface reaction between Ce and the CeO_2 buffer are continuous and free of Cu. However, the oxidation of the continuous layer of reduced ceria on Cu may eventually expose the ceria–copper interface which must be accounted for when evaluating the chemical reactivity of such layers.

The STM images in Figure 5 are presented as illuminated from the right to enhance the surface texture on the terraces related to the respective surface reconstruction. This texture is most pronounced for the (4×4) reconstructed samples of Ce_2O_3 (Figure 5(c) and the inset of Figure 5(c)). After oxidation of the Ce_2O_3 layer the texture vanishes, and the surface converts to the (1×1) reconstruction (Figure 5(d) and the inset of Figure 5(d)). For samples with the $(\sqrt{7} \times \sqrt{7})\text{R}19.1^\circ$ surface reconstruction the STM images show streaks indicative of instability of the surface in the tunneling contact. The surface texture cannot be resolved in STM (Figure

5(b) and the inset of Figure 5(b)). The same instability is observed on the samples with the (3×3) surface reconstruction. The instability in STM is a property of the $(\sqrt{7} \times \sqrt{7})\text{R}19.1^\circ$ and (3×3) surface reconstructions independent of the imaging condition of the STM tip. On the samples where $(\sqrt{7} \times \sqrt{7})\text{R}19.1^\circ$ and/or (3×3) surface reconstructions coexist with the (4×4) reconstruction, the areas with (4×4) reconstruction appear stable and well resolved next to the instable areas with $(\sqrt{7} \times \sqrt{7})\text{R}19.1^\circ$ and/or (3×3) reconstructions in the same STM image.

DISCUSSION

Reduction of ceria films by the interface reaction with Ce eventually complemented by oxidation with O_2 allows us to prepare ceria thin films on Cu(111) in the whole range of stoichiometries between CeO_2 and Ce_2O_3 . The films exhibit four distinct surface reconstructions, (1×1) (CeO_2), $(\sqrt{7} \times \sqrt{7})\text{R}19.1^\circ$, (3×3) , and (4×4) (Ce_2O_3) as identified by LEED. The discussion of our experiment is devoted to the following aspects: (i) We give arguments that all the observed surface reconstructions are based on ordering of oxygen vacancies in cubic fluorite-like ceria, (ii) we estimate the stoichiometry and propose a model of the (3×3) surface reconstruction, (iii) we estimate and rationalize the depth profile of the vacancy concentration in the $(\sqrt{7} \times \sqrt{7})\text{R}19.1^\circ$ and (3×3) reconstructed layers, and (iv) we propose a mechanism leading to the nucleation of the cubic ceria phase during reduction of ceria layers via the interface reaction with Ce. In our arguments we recall the experimental observation of Perkins et al.⁴³ concerning the bulk mobility of O and Ce atoms in fluorite-like ceria: At temperatures around 600°C corresponding to the annealing temperature in our experiment, Ce atoms are virtually immobile in the ceria bulk, while O atoms are already highly mobile, their bulk mobility being released at temperatures as low as 300°C .⁴³ In terms of this observation, we are viewing all changes in the ordered reduced ceria layers in our experiment as creation, annihilation, and equilibration of oxygen vacancies in a relatively rigid frame of cubic ceria.

(i) There is a strong experimental evidence of ordering of oxygen vacancies in bulk reduced ceria (ref 44 and references therein), and several phases of bulk reduced ceria with stoichiometries approximately between $\text{CeO}_{1.81}$ and $\text{CeO}_{1.66}$ have been identified in neutron diffraction experiments.^{26,28} These phases are obtained by removing oxygen atoms from the fluorite lattice of CeO_2 and ordering of the resulting oxygen vacancies to superstructures with distinct spatial correlations.²⁸ Recently, two of these bulk structures have been employed successfully in explaining the reconstructions observed in LEED on thin films of reduced ceria. The $(\sqrt{7} \times \sqrt{7})\text{R}19.1^\circ$ LEED pattern on a layer of CeO_x was associated with a bulk termination of the $t\text{-Ce}_7\text{O}_{12}$ phase.^{26,29} The (4×4) LEED pattern on a layer of Ce_2O_3 was associated with a bulk termination of the $c\text{-Ce}_2\text{O}_{3+\delta}$ phase^{28,30} that was realized for $\delta = 0$ as a thin film of $c\text{-Ce}_2\text{O}_3$ on Cu(111). Both $(\sqrt{7} \times \sqrt{7})\text{R}19.1^\circ$ and (4×4) reconstructions are realized in the present experiments as well. Further, the present experiments reveal a (3×3) surface reconstruction for ceria layers that are according to XPS and RPES more reduced than $(\sqrt{7} \times \sqrt{7})\text{R}19.1^\circ$ terminated layers but less reduced than (4×4) terminated layers (cf. Figures 1–3). We propose that the (3×3) terminated phase can be derived from bulk ordering of oxygen vacancies in cubic ceria as well. The main argument for

our proposal is the observation that the (3×3) terminated phase can be obtained by oxidation of the cubic Ce_2O_3 (4×4) phase at temperatures when the Ce atoms are virtually immobile (cf. Figures 2 and 3 and Perkins et al.⁴³).

(ii) With this evidence for the cubic structure of the (3×3) surface reconstruction we can propose the microscopic model of this reconstruction in analogy with the models of $(\sqrt{7} \times \sqrt{7})\text{R}19.1^\circ$ and (4×4) reconstructions. All models for the surface reconstructions observed in our experiments are displayed in Figure 6. The models are presented as top views

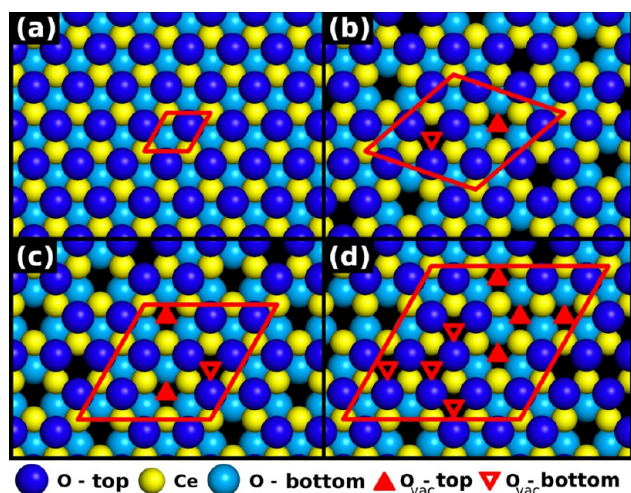


Figure 6. Schematic top view of the ordered phases of reduced ceria on Cu(111). Images represent one monolayer from the related bulk structure. (a) $\text{CeO}_2(111)$ corresponding to the LEED pattern (1×1) on Figure 1(a), bulk structure ICSD #169029. (b) $\text{CeO}_{1.71}$ corresponding to the LEED pattern $(\sqrt{7} \times \sqrt{7})\text{R}19.1^\circ$ on Figure 1(b), bulk structure PCD #1805255. (c) $\text{CeO}_{1.67}$ corresponding to the LEED pattern (3×3) on Figure 1(c), proposal of the present work. (d) $\text{c-Ce}_2\text{O}_3(111)$ corresponding to the LEED pattern (4×4) on Figure 1(d), bulk structure ICSD #96202. Surface unit cells are highlighted by a red line, and top and bottom O vacancies are highlighted by full and empty red triangles, respectively.

of one monolayer of ceria oriented in the (111) direction of the fluorite lattice corresponding to a particular bulk model of the reduced ceria. When available, the bulk models are adopted from crystallographic databases, the Inorganic Crystal Structure Database (ICSD), and the Pearson's Crystal Data Crystal Structure Database for Inorganic Compounds (PCD). Figure 6(a) displays the reference (111) plane of CeO_2 (bulk model ICSD #169029). Figure 6(b) displays the corresponding cut through the bulk $\text{CeO}_{1.71}$ phase (PCD #1805255) according to Wilkens et al.²⁹ and Figure 6(d) the cut through the bulk $\text{c-Ce}_2\text{O}_3$ phase (ICSD #96202) according to Stetsovych et al.³⁰ In the figures, the surface unit cell corresponding to the LEED patterns of (1×1) (Figure 6(a)), $(\sqrt{7} \times \sqrt{7})\text{R}19.1^\circ$ (Figure 6(b)), and (4×4) (Figure 6(d)) is outlined red and the positions of the oxygen vacancies in the upper and lower O layers in the ceria monolayer by full and empty red triangles, respectively.

For the model of the (3×3) reconstruction we have to estimate the number and the positions of the oxygen vacancies in the (3×3) surface unit cell relative to $\text{CeO}_2(111)$. According to the XPS measurements (Figure 3), the stoichiometry of the (3×3) surface reconstruction is intermediate between the $(\sqrt{7} \times \sqrt{7})\text{R}19.1^\circ$ ($\text{CeO}_{1.71}$ or

$\text{CeO}_{1.71}$) and the (4×4) ($\text{c-Ce}_2\text{O}_3$ or $\text{CeO}_{1.5}$) reconstructions. According to RPES measurements (Figure 4) the stoichiometry of the (3×3) reconstruction is close to the $(\sqrt{7} \times \sqrt{7})\text{R}19.1^\circ$ ($\text{CeO}_{1.71}$) reconstruction. Therefore, we propose that the (3×3) surface unit cell includes three oxygen vacancies corresponding to the model stoichiometry $\text{CeO}_{1.67}$. Regarding the positions of the oxygen vacancies in the model of the (3×3) reconstruction, we recall the preferential orientations of vacancy pairs in ceria bulk observed and analyzed in neutron diffraction experiments.²⁸ Particularly, oxygen vacancies in the bulk tend to repel each other and show a strong preference for certain spatial correlations. These rules for vacancy ordering determine the models of the $(\sqrt{7} \times \sqrt{7})\text{R}19.1^\circ$ surface reconstruction (Figure 6(b)) and the (4×4) surface reconstruction (Figure 6(d)). The (3×3) surface reconstruction cannot be identified as a simple cut through any of the established models of bulk reduced ceria; however, the oxygen vacancies can be positioned in the preferred mutual positions as well. This is shown in our proposal for the model of the (3×3) reconstruction in Figure 6(c). The spatial correlations of vacancies in the model of the (3×3) reconstruction are those appearing in the models of the $(\sqrt{7} \times \sqrt{7})\text{R}19.1^\circ$ and the (4×4) reconstructions, too.

We have to note that the models of the reduced ceria surfaces derived from the bulk phases of reduced ceria have to be considered only as suggestions plausibly explaining the superstructures observed in LEED and subject to further refinement by microscopic, diffraction, and ab initio techniques. The rules governing the ordering of the oxygen vacancies on the surfaces of reduced ceria seem to be still more complex. Indeed, oxygen vacancies observed on the reduced ceria surfaces by microscopic techniques adopt spatial correlations that are not realized in the bulk. Esch et al.²² observe and rationalize based on ab initio calculations a stabilization of surface vacancy chains by a subsurface vacancy corresponding to a $(0,0,1)$ vacancy pair in the notation of Kümmerle and Heger. Torbrugge et al.⁴⁵ observe and Murgida and Ganduglia-Pirovano⁴⁶ rationalize based on ab initio calculations a stabilization of subsurface vacancies as $(0,2,2)$ vacancy pairs. Both $(0,0,1)$ and $(0,2,2)$ vacancy pairs are not realized in bulk samples.²⁸

Unfortunately, microscopic evidence for the vacancy distribution on $(\sqrt{7} \times \sqrt{7})\text{R}19.1^\circ$ and (3×3) terminated samples was not obtained in this work due to an inherent instability of the STM images of the $(\sqrt{7} \times \sqrt{7})\text{R}19.1^\circ$ (Figure 5(b)) and (3×3) reconstructions in our experimental setup. Since in comparable STM experiments the surface vacancies on ceria seem to be immobile,^{22,47} we assign the instability of the STM images to water molecules accumulating on the $(\sqrt{7} \times \sqrt{7})\text{R}19.1^\circ$ and (3×3) surfaces in our STM during the prolonged measuring sessions without the possibility of flash heating of the samples.

(iii) The models of the $(\sqrt{7} \times \sqrt{7})\text{R}19.1^\circ$ and (3×3) surface reconstructions of the reduced ceria layers in our experiment predict the stoichiometry of the corresponding reduced bulk phases $\text{CeO}_{1.71}$ and $\text{CeO}_{1.67}$, respectively. For the comparison with the experiment we have to realize the different information depth of the employed experimental methods for determining the stoichiometry. The overview of the stoichiometry of the layers with the $(\sqrt{7} \times \sqrt{7})\text{R}19.1^\circ$ and (3×3) surface reconstructions (Figure 1) measured by XPS at normal emission (Figures 2 and 3), XPS at 70° off normal emission (Figures 2 and 3), and RPES (Figure 4) in comparison with the

predicted stoichiometry (Figure 6) is presented in Table 2. We observe that the predicted and the measured values of the

Table 2. Stoichiometries Determined from Experiments with Different Information Depth

reconstruction (Figure 1)	x in CeO_x			
	XPS 0° (Figure 2)	XPS 70° (Figure 2)	RPES (Figure 4)	model (Figure 6)
$(\sqrt{7} \times \sqrt{7})\text{R}19.1^\circ$	1.86	1.82	1.67	1.71 ²⁹
(3×3)	1.78	1.70	1.65	1.67

stoichiometry of the layers correspond reasonably well only for the most surface-sensitive measurement by RPES. Measurements by XPS show stoichiometries that are less reduced than expected. The experimentally determined degree of reduction decreases with the increasing information depth of the employed experimental method. This suggests that the reduced ceria phases Ce_7O_{12} and $\text{CeO}_{1.67}$ are floating on a more oxidized ceria.

We propose that the enhancement of the concentration of the oxygen vacancies near the surface of the reduced ceria films represents a general effect resulting from equilibrium distribution of the oxygen vacancies in thin CeO_x films. The equilibrium is indicated by the independence on the preparation history of the samples (Figure 3). The enhanced concentration of surface vacancies is observed for the samples prepared both by reduction of CeO_2 by Ce and by oxidation of Ce_2O_3 by O_2 . The equilibration is mediated by a high mobility of oxygen atoms and oxygen vacancies in the CeO_x thin films at temperatures well below the annealing temperature of 600 °C used during the sample preparation in the present study.⁴³ Oxygen vacancies near the surface are thermodynamically favorable as predicted by theoretical calculations.^{48,49} Oxygen vacancies may also respond sensitively to the strain in the ceria film. Oxygen vacancies expand the lattice parameter of the reduced ceria due to a larger diameter of the associated Ce^{3+} cations compared to the Ce^{4+} cations in the oxidized ceria.^{30,44} The presence of the ceria–Cu(111) interface in the metal-supported thin ceria film on the other hand induces a contraction of the lattice parameter of ceria.^{50,51} The interplay between these two effects ultimately results in a force driving the oxygen vacancies away from the ceria–Cu(111) interface and toward the surface of the film. The enhancement of the oxygen vacancy concentration near the surface of ceria was predicted and observed also in ceria nanoparticles.^{52,53}

The change of the vacancy concentration with the distance from the surface of the reduced ceria is most likely continuous, but we can estimate a characteristic length scale over which the change of the vacancy concentration is taking place using a simple two-level model of ref 54. This model assumes a homogeneous layer of reduced ceria (in our case with the stoichiometry $\text{CeO}_{1.71}$ or $\text{CeO}_{1.67}$) floating on the homogeneous CeO_2 . The thickness of the reduced ceria layer can then be determined from XPS measurements at normal emission using the following equation:⁵⁴ $I_s(\text{Ce}_{\text{composite}}^{4+}) - I_s(\text{Ce}_{\text{overlayer}}^{4+}) = I_s(\text{Ce}_{\text{buffer}}^{4+})\exp(-(d/\lambda))$, where $I_s(\text{Ce}_{\text{composite}}^{4+})$ is the Ce^{4+} signal measured on the reduced layers, $(\text{Ce}_{\text{overlayer}}^{4+})$ is the simulated Ce^{4+} signal corresponding to the $\text{CeO}_{1.71}$ or $\text{CeO}_{1.67}$ overlayer computed from the measured Ce^{3+} signal and the expected stoichiometry of the overlayer, $I_s(\text{Ce}_{\text{buffer}}^{4+})$ is the Ce^{4+} signal from the CeO_2 buffer layer (in the case of the films prepared by oxidation the signal from fully oxidized film is used instead), d

is the thickness of the $\text{CeO}_{1.71}$ or $\text{CeO}_{1.67}$ overlayers, and λ is the inelastic mean free path in the reduced layers. The results of this simple estimation show that the samples with the $(\sqrt{7} \times \sqrt{7})\text{R}19.1^\circ$ reconstruction consist of 2–3 ML of $\text{CeO}_{1.71}$ supported by CeO_2 , and the samples with the (3×3) reconstruction consist of 3–4 ML of $\text{CeO}_{1.67}$ supported by CeO_2 .

(iv) The observation of the cubic structure of the ceria layers in our experiment in the whole range of stoichiometries between CeO_2 and Ce_2O_3 is allowed by the special property of the alternative method of reduction of ceria by the reaction with metallic Ce to yield the cubic structure even for the limiting reduction to Ce_2O_3 where hexagonal Ce_2O_3 is the lowest-energy configuration.^{41,55,56} We propose a model for the stabilization of the cubic reduced ceria in the interface reaction. The illustration of this model is in Figure 7. A starting point is

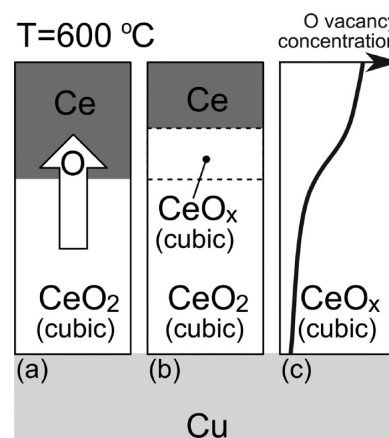


Figure 7. Schematic drawing of the interface reaction upon deposition of metallic Ce (dark gray) on ceria buffer layer (white) on the Cu(111) substrate (light gray) and heating the system to 600 °C. (a) O diffuses from the ceria buffer to oxidize the Ce deposit. (b) Oxidized Ce in the deposit adopts the cubic structure of the buffer. (c) O vacancies in the resulting layer equilibrate establishing a concentration gradient with maximum of O vacancies near the surface.

the deposition of Ce metal on the cubic ceria buffer. The cubic ceria buffer is available in all our experiments, cf. Figures 2 and 3 and Table 1. After heating to 600 °C, oxygen from the ceria buffer diffuses into the Ce overlayer and oxidizes it (Figure 7(a)). The oxidized Ce in the overlayer adopts the cubic structure of the buffer that acts as a nucleation template. In this way, the system also avoids an energy increase associated with an eventual nucleation of an interface between the cubic and the hexagonal ceria (Figure 7(b)). Finally, upon oxidation of the Ce overlayer that establishes the cubic structure in the film the oxygen vacancies adopt an equilibrium distribution with a maximum of concentration near the surface of the film (Figure 7(c)). The gradient of distribution of oxygen vacancies is not observed for the samples with the limiting stoichiometry— CeO_2 and Ce_2O_3 (Figure 3)—because in these samples the vacancies occupy no (in CeO_2) or all (in Ce_2O_3) available positions. During transitions between CeO_2 and Ce_2O_3 the ordered thin film of reduced ceria must adapt to the accompanying changes of the ceria lattice constant.³⁰ On Cu(111), this adaptation is facilitated by the incommensurate character of growth of ceria on Cu(111) and by the ability of ceria films to glide on the Cu(111) substrate.⁵⁷

CONCLUSIONS

We have performed a detailed study of the properties of thin films of reduced ceria on Cu(111) prepared by the interfacial reaction between a ceria thin film and a Ce metal deposit. Thin films of reduced ceria are continuous and completely cover the Cu substrate. Controlling the amount of Ce in the interfacial reaction we can prepare thin films of reduced ceria with stoichiometry changing continuously between CeO₂ and Ce₂O₃. The change in the stoichiometry is accompanied by changes in the surface reconstruction of the films. Starting from the (1 × 1) reconstruction of CeO₂ and increasing the degree of reduction we observe ($\sqrt{7} \times \sqrt{7}$)R19.1° and (3 × 3) reconstructions of CeO_x and, finally, the (4 × 4) reconstruction of cubic Ce₂O₃. In the films with stoichiometry between CeO₂ and Ce₂O₃ the oxygen vacancies accumulate near the surface of the films.

We observe that the process of reduction of thin ceria films by the interfacial reaction with Ce is fully reversible upon oxidation with O₂. This reversibility covers all properties of the reduced ceria thin films including the surface reconstructions and the depth profile of oxygen vacancies. This allows us to discuss the properties of the ceria layers in terms of equilibration of mobile oxygen vacancies in a relatively rigid cubic lattice of cerium atoms. The cubic structure of the reduced ceria layers is established during the interface reaction with Ce. Oxygen vacancies are driven away from the Cu(111)–ceria interface to relieve the stress associated with the expansion of the lattice constant during the reduction of ceria. The ($\sqrt{7} \times \sqrt{7}$)R19.1° and (3 × 3) reconstructions are identified as surface terminations of ordered bulk phases of reduced ceria, the *ν*-Ce₇O₁₂ or CeO_{1.71} phase for the ($\sqrt{7} \times \sqrt{7}$)R19.1° reconstruction, and the CeO_{1.67} phase for the (3 × 3) reconstruction. These bulk reduced phases representing distinct regular arrangements of oxygen vacancies in cubic ceria are established in the three topmost monolayers of the reduced ceria films.

Practically, ceria layers reduced by the interface reaction with metallic Ce represent a realization of the ideal scenario of reduction and reoxidation of ceria by removing/adding O from/to the fluorite CeO₂ lattice without largely modifying the structure of the Ce sublattice.⁹ This, accompanied by the preference of oxygen vacancies to arrange in regular structures, makes the ceria layers reduced by interface reaction with metallic Ce a unique experimental playground for studying the influence of the oxygen vacancy concentration and coordination on the chemical properties of ceria.

AUTHOR INFORMATION

Corresponding Author

*E-mail: josef.myslivecek@mff.cuni.cz. Phone: +420 221 912 333. Fax: +420 284 685 095.

Notes

The authors declare no competing financial interest.

ACKNOWLEDGMENTS

This work was supported by the Czech Science Foundation (GAČR P204-11-1183, GAČR 13-10396S) and by the Ministry of Education of the Czech Republic (LG12003, LH11017). T.D., F.D., M.A., and V.S. acknowledge the support of the Grant Agency of the Charles University (GAUK 794313, GAUK 610112, GAUK 320313, GAUK 339311). We would

also like to thank Radomír Kužel for the discussion of ICSD and PCD data.

REFERENCES

- (1) Trovarelli, A.; de Leitenburg, C.; Boaro, M.; Dolcetti, G. The Utilization of Ceria in Industrial Catalysis. *Catal. Today* **1999**, *50*, 353–367.
- (2) Diebold, U. The Surface Science of Titanium Dioxide. *Surf. Sci. Rep.* **2003**, *48*, 53–229.
- (3) Wachs, I. E. Catalysis Science of Supported Vanadium Oxide Catalysts. *Dalton Trans.* **2013**, *42*, 11762–11769.
- (4) Carabineiro, S. A. C.; Bogdanchikova, N.; Tavares, P. B.; Figueiredo, J. L. Nanostructured Iron Oxide Catalysts with Gold for the Oxidation of Carbon Monoxide. *RSC Adv.* **2012**, *2*, 2957–2965.
- (5) Rosen, J.; Hutchings, G. S.; Jiao, F. Ordered Mesoporous Cobalt Oxide as Highly Efficient Oxygen Evolution Catalyst. *J. Am. Chem. Soc.* **2013**, *135*, 4516–4521.
- (6) Gorlin, Y.; Lassalle-Kaiser, B.; Benck, J. D.; Gul, S.; Webb, S. M.; Yachandra, V. K.; Yano, J.; Jaramillo, T. F. In Situ X-ray Absorption Spectroscopy Investigation of a Bifunctional Manganese Oxide Catalyst with High Activity for Electrochemical Water Oxidation and Oxygen Reduction. *J. Am. Chem. Soc.* **2013**, *135*, 8525–8534.
- (7) Borchert, Y.; Sonström, P.; Wilhelm, M.; Borchert, H.; Bäumer, M. Nanostructured Praseodymium Oxide: Preparation, Structure, and Catalytic Properties. *J. Phys. Chem. C* **2008**, *112*, 3054–3063.
- (8) Schubert, M. CO Oxidation over Supported Gold Catalysts – “Inert” and “Active” Support Materials and Their Role for the Oxygen Supply during Reaction. *J. Catal.* **2001**, *197*, 113–122.
- (9) Skorodumova, N.; Simak, S.; Lundqvist, B.; Abrikosov, I.; Johansson, B. Quantum Origin of the Oxygen Storage Capability of Ceria. *Phys. Rev. Lett.* **2002**, *89*, 166601.
- (10) Maezono, R.; Ishihara, S.; Nagaosa, N. Phase Diagram of Manganese Oxides. *Phys. Rev. B* **1998**, *58*, 11583–11596.
- (11) Ketteler, G.; Weiss, W.; Ranke, W.; Schlögl, R. Bulk and Surface Phases of Iron Oxides in an Oxygen and Water Atmosphere at Low Pressure. *Phys. Chem. Chem. Phys.* **2001**, *3*, 1114–1122.
- (12) Waldner, P.; Eriksson, G. Thermodynamic Modelling of the System Titanium–Oxygen. *CALPHAD: Comput. Coupling Phase Diagrams Thermochem.* **1999**, *23*, 189–218.
- (13) Zinkevich, M.; Djurovic, D.; Aldinger, F. Thermodynamic Modelling of the Cerium–Oxygen System. *Solid State Ionics* **2006**, *177*, 989–1001.
- (14) Katzke, H.; Tolédano, P.; Depmeier, W. Theory of Morphotropic Transformations in Vanadium Oxides. *Phys. Rev. B* **2003**, *68*, 024109.
- (15) Ruh, L.; Patel, V. A. Proposed Phase Relations in the HfO₂-Rich Portion of the system Hf–HfO₂. *J. Am. Ceram. Soc.* **1973**, *56*, 606–607.
- (16) Ferro, S. Physicochemical and Electrical Properties of Praseodymium Oxides. *Int. J. Electrochem.* **2011**, *2011*, 1–7.
- (17) Arroyave, R.; Kaufman, L.; Eagar, T. Thermodynamic Modeling of the Zr–O System. *CALPHAD: Comput. Coupling Phase Diagrams Thermochem.* **2002**, *26*, 95–118.
- (18) Sonström, P.; Birkenstock, J.; Borchert, Y.; Schilinsky, L.; Behrend, P.; Gries, K.; Müller, K.; Rosenauer, A.; Bäumer, M. Nanostructured Praseodymium Oxide: Correlation Between Phase Transitions and Catalytic Activity. *ChemCatChem* **2010**, *2*, 694–704.
- (19) Franchini, C.; Podloucky, R.; Allegretti, F.; Li, F.; Parteder, G.; Surnev, S.; Netzer, F. Structural and Vibrational Properties of Two-Dimensional Mn₂O₇ Layers on Pd(100): Experiments and Density Functional Theory Calculations. *Phys. Rev. B* **2009**, *79*, 035420.
- (20) Biedermann, K.; Gubo, M.; Hammer, L.; Heinz, K. Phases and Phase Transitions of Hexagonal Cobalt Oxide Films on Ir(100)-(1 × 1). *J. Phys.: Condens. Matter* **2009**, *21*, 185003.
- (21) Ketteler, G.; Ranke, W. Heteroepitaxial Growth and Nucleation of Iron Oxide Films on Ru(0001). *J. Phys. Chem. B* **2003**, *107*, 4320–4333.
- (22) Esch, F.; Fabris, S.; Zhou, L.; Montini, T.; Africh, C.; Fornasiero, P.; Comelli, G.; Rosei, R. Electron Localization Determines Defect Formation on Ceria Substrates. *Science* **2005**, *309*, 752–755.

- (23) Ganduglia-Pirovano, M. V.; Hofmann, A.; Sauer, J. Oxygen Vacancies in Transition Metal and Rare Earth Oxides: Current State of Understanding and Remaining Challenges. *Surf. Sci. Rep.* **2007**, *62*, 219–270.
- (24) Lawrence, N. J.; Brewer, J. R.; Wang, L.; Wu, T.-S.; Wells-Kingsbury, J.; Ihrig, M. M.; Wang, G.; Soo, Y.-L.; Mei, W.-N.; Cheung, C. L. Defect Engineering in Cubic Cerium Oxide Nanostructures for Catalytic Oxidation. *Nano Lett.* **2011**, *11*, 2666–2671.
- (25) Senanayake, S. D.; Stacchiola, D.; Evans, J.; Estrella, M.; Barrio, L.; Pérez, M.; Hrbek, J.; Rodriguez, J. A. Probing the Reaction Intermediates for the Water-gas Shift over Inverse $\text{CeO}_x/\text{Au}(111)$ catalysts. *J. Catal.* **2010**, *271*, 392–400.
- (26) Ray, S.; Cox, D. Neutron Diffraction Determination of the Crystal Structure of Ce_7O_{12} . *J. Solid State Chem.* **1975**, *15*, 333–343.
- (27) Knappe, P.; Eyring, L. Preparation and Electron Microscopy of Intermediate Phases in the Interval Ce_7O_{12} – $\text{Ce}_{11}\text{O}_{20}$. *J. Solid State Chem.* **1985**, *58*, 312–324.
- (28) Kümmerle, E.; Heger, G. The Structures of $c\text{-Ce}_2\text{O}_{3+\delta}$, Ce_7O_{12} , and $\text{Ce}_{11}\text{O}_{20}$. *J. Solid State Chem.* **1999**, *147*, 485–500.
- (29) Wilkens, H.; Schuckmann, O.; Oelke, R.; Gevers, S.; Schaefer, A.; Bäumer, M.; Zoellner, M. H.; Schroeder, T.; Wollschläger, J. Stabilization of the Ceria ι -phase (Ce_7O_{12}) surface on $\text{Si}(111)$. *Appl. Phys. Lett.* **2013**, *102*, 111602.
- (30) Stetsovych, V.; Pagliuca, F.; Dvořák, F.; Duchoň, T.; Vorokhta, M.; Aulická, M.; Lachnitt, J.; Schernich, S.; Matolínová, I.; Veltruská, K.; et al. Epitaxial Cubic Ce_2O_3 Films via Ce – CeO_2 Interfacial Reaction. *J. Phys. Chem. Lett.* **2013**, *4*, 866–871.
- (31) Wilkens, H.; Schuckmann, O.; Oelke, R.; Gevers, S.; Reichling, M.; Schaefer, A.; Bäumer, M.; Zoellner, M. H.; Niu, G.; Schroeder, T.; et al. Structural Transitions of Epitaxial Ceria Films on $\text{Si}(111)$. *Phys. Chem. Chem. Phys.* **2013**, *15*, 18589–99.
- (32) Dvořák, F.; Stetsovych, O.; Steger, M.; Cherradi, E.; Matolínová, I.; Tsud, N.; Škoda, M.; Skála, T.; Mysliveček, J.; Matolín, V. Adjusting Morphology and Surface Reduction of $\text{CeO}_2(111)$ Thin Films on $\text{Cu}(111)$. *J. Phys. Chem. C* **2011**, *115*, 7496–7503.
- (33) Tanuma, S.; Powell, C. J.; Penn, D. R. Calculation of Electron Inelastic Mean Free Paths (IMFPs) VII. Reliability of the TPP-2M IMFP Predictive Equation. *Surf. Interface Anal.* **2003**, *35*, 268–275.
- (34) Skála, T.; Šutara, F.; Prince, K. C.; Matolín, V. Cerium Oxide Stoichiometry Alteration via Sn Deposition: Influence of Temperature. *J. Electron Spectrosc. Relat. Phenom.* **2009**, *169*, 20–25.
- (35) Pagliuca, F.; Luches, P.; Valeri, S. Interfacial Interaction between Cerium Oxide and Silicon Surfaces. *Surf. Sci.* **2013**, *607*, 164–169.
- (36) Powell, C.; Jablonski, A.; Tilinin, I.; Tanuma, S.; Penn, D. Surface Sensitivity of Auger-electron Spectroscopy and X-ray Photoelectron Spectroscopy. *J. Electron Spectrosc. Relat. Phenom.* **1999**, *98*, 1–15.
- (37) Matolín, V.; Cabala, M.; Cháb, V.; Matolínová, I.; Prince, K. C.; Škoda, M.; Šutara, F.; Skála, T.; Veltruská, K. A Resonant Photoelectron Spectroscopy Study of $\text{Sn}(\text{Ox})$ Doped CeO_2 Catalysts. *Surf. Interface Anal.* **2008**, *40*, 225–230.
- (38) Albrecht, P. M.; Mullins, D. R. Adsorption and Reaction of Methanol Over $\text{CeO}_x(100)$ Thin Films. *Langmuir* **2013**, *29*, 4559–4567.
- (39) Mullins, D. R.; Overbury, S. H.; Huntley, D. R. Electron Spectroscopy of Single Crystal and Polycrystalline Cerium Oxide Surfaces. *Surf. Sci.* **1998**, *409*, 307–319.
- (40) Castellarin-Cudia, C.; Surnev, S.; Schneider, G.; Podlucky, R.; Ramsey, M.; Netzer, F. Strain-induced Formation of Arrays of Catalytically Active Sites at the Metal-Oxide Interface. *Surf. Sci.* **2004**, *554*, L120–L126.
- (41) Vescovo, E.; Carbone, C. Oxidation of Epitaxial Ce Films. *Phys. Rev. B* **1996**, *53*, 4142–4147.
- (42) Mudiyaanselage, K.; Senanayake, S. D.; Feria, L.; Kundu, S.; Baber, A. E.; Graciani, J.; Vidal, A. B.; Agnoli, S.; Evans, J.; Chang, R.; et al. Importance of the Metal-Oxide Interface in Catalysis: In Situ Studies of the Water-Gas Shift Reaction by Ambient-pressure X-ray Photoelectron Spectroscopy. *Angew. Chem., Int. Ed. Engl.* **2013**, *52*, 5101–5105.
- (43) Perkins, C. L.; Henderson, M. A.; Peden, C. H. F.; Herman, G. S. Self-Diffusion in Ceria. *J. Vac. Sci. Technol., A* **2001**, *19*, 1942–1946.
- (44) Trovarelli, A. *Catalysis by Ceria and Related Materials*; Imperial College Press: London, 2002.
- (45) Torbrügge, S.; Reichling, M.; Ishiyama, A.; Morita, S.; Custance, O. Evidence of Subsurface Oxygen Vacancy Ordering on Reduced $\text{CeO}_2(111)$. *Phys. Rev. Lett.* **2007**, *99*, 056101.
- (46) Murgida, G. E.; Ganduglia-Pirovano, M. V. Evidence for Subsurface Ordering of Oxygen Vacancies on the Reduced $\text{CeO}_2(111)$ Surface Using Density-Functional and Statistical Calculations. *Phys. Rev. Lett.* **2013**, *110*, 246101.
- (47) Zhou, Y.; Perket, J. M.; Zhou, J. Growth of Pt Nanoparticles on Reducible $\text{CeO}_2(111)$ Thin Films: Effect of Nanostructures and Redox Properties of Ceria. *J. Phys. Chem. C* **2010**, *114*, 11853–11860.
- (48) Conesa, J. Computer Modeling of Surfaces and Defects on Cerium Dioxide. *Surf. Sci.* **1995**, *339*, 337–352.
- (49) Paier, J.; Penschke, C.; Sauer, J. Oxygen Defects and Surface Chemistry of Ceria: Quantum Chemical Studies Compared to Experiment. *Chem. Rev.* **2013**, *113*, 3949–3985.
- (50) Szabová, L.; Stetsovych, O.; Dvořák, F.; Farnesi Camellone, M.; Fabris, S.; Mysliveček, J.; Matolín, V. Distinct Physicochemical Properties of the First Ceria Monolayer on $\text{Cu}(111)$. *J. Phys. Chem. C* **2012**, *116*, 6677–6684.
- (51) Mašek, K.; Beran, J.; Matolín, V. RHEED Study of the Growth of Cerium Oxide on $\text{Cu}(111)$. *Appl. Surf. Sci.* **2012**, *259*, 34–38.
- (52) Loschen, C.; Migani, A.; Bromley, S. T.; Illas, F.; Neyman, K. M. Density Functional Studies of Model Cerium Oxide Nanoparticles. *Phys. Chem. Chem. Phys.* **2008**, *10*, 5730–5738.
- (53) Turner, S.; Lazar, S.; Freitag, B.; Egoavil, R.; Verbeeck, J.; Put, S.; Strauven, Y.; Van Tendeloo, G. High Resolution Mapping of Surface Reduction in Ceria Nanoparticles. *Nanoscale* **2011**, *3*, 3385–3390.
- (54) Wang, G.; Kong, D.; Pan, Y.; Pan, H.; Zhu, J. Low Energy Ar-Ion Bombardment Effects on the CeO_2 Surface. *Appl. Surf. Sci.* **2012**, *258*, 2057–2061.
- (55) Da Silva, J. Stability of the Ce_2O_3 Phases: A DFT+U Investigation. *Phys. Rev. B* **2007**, *76*, 193108.
- (56) Xiao, W.; Guo, Q.; Wang, E. Transformation of $\text{CeO}_2(111)$ to $\text{Ce}_2\text{O}_3(0001)$ Films. *Chem. Phys. Lett.* **2003**, *368*, 527–531.
- (57) Stetsovych, O.; Dvořák, F.; Szabová, L.; Fabris, S.; Mysliveček, J.; Matolín, V. Nanometer-Range Strain Distribution in Layered Incommensurate Systems. *Phys. Rev. Lett.* **2012**, *109*, 266102.